Soft Matter

Cite this: *Soft Matter*, 2012, **8**, 2697

www.rsc.org/softmatter

**PAPER**

# Polymer–inorganic hybrid microparticles with hierarchical structures formed by interfacial instabilities of emulsion droplets†

**Naixiang Wang, Yonggui Liao, Renhua Deng, Shanqin Liu, Nan Cao, Bien Tan, Jintao Zhu* and Xiaolin Xie**

***Received 1st October 2011, Accepted 7th December 2011***
**DOI: 10.1039/c2sm06874e**



We introduce a facile, yet robust route for fabricating polymer–inorganic hybrid microparticles with hierarchically-structured morphologies by taking advantage of the interfacial instabilities of emulsion droplets and the sol–gel chemistry of silica precursors. In general, chloroform-in-water emulsion droplets containing an amphiphilic diblock copolymer [polystyrene-*b*-poly (ethylene oxide) (PS–PEO)] and metal oxide precursors [tetraethyl orthosilicate (TEOS) or mixtures of TEOS and tetra-*tert*-butyl orthotitanate (TBOT)] were prepared by shaking. Upon solvent evaporation, interfacial instabilities occurred while the inorganic precursors started to hydrolyze and condense when brought in contact with the aqueous solution, ultimately leading to the formation of a mineralized shell at the oil–water interface and hybrid microparticles. By varying the rate of solvent evaporation, qualitatively different mechanisms of the instabilities (*e.g.*, the budding of vesicles or a spines-to-vesicles transition) were observed. The effect of the synthesis conditions, such as the amount of TEOS, the solvent evaporation rate, and the pH value on the self-assembly of the copolymer, the interfacial behavior of the solvent/water, and the morphology of the microparticles were investigated. Hierarchical microparticles with different morphologies, ranging from cage-like, honeycomb-like, dendritic, to budded microparticles, were prepared by combining the sol–gel process with the self-assembly of the polymers in the emulsion droplets. Moreover, the intermediate structures of the instabilities were kinetically trapped by the mineralization process. Our study indicated that the hybrid microparticles formed by interfacial instabilities of emulsion droplets can significantly expand the range of accessible morphologies, which provides the potential for advanced applications in drug storage, coatings, controlled release, and catalysis.

## Introduction

Amphiphilic block copolymers can self-assemble into a variety of supramolecular structures in the form of spherical or wormlike micellar, vesicular, and more complex microstructures, depending on polymer chemistry (such as molecular weight, block ratio, and chemistry) and processing conditions (*e.g.*, solvent properties, initial polymer concentration, ionic strength, and temperature).[1–8] Such self-assembled structures provide functional platforms for the design of organic–inorganic hybrid and mesoporous materials with outstanding properties, potentially useful in the fields of catalyst host, molecular separation, diagnostics, bioimaging, among others.[9–18] Most of the synthesis routes are based on either hydrothermal processing or sol–gel chemistry in combination with the template approach.[16,19–21] In the sol–gel process, appropriate precursors, mostly alkoxides, are transformed into silica by hydrolysis and condensation in an aqueous phase.[16,22–25] Recently, Armes and colleagues used cationic diblock copolymer micelles as colloidal templates for the deposition of silica at ambient temperature, leading to the formation of hybrid polymer–silica nanoparticles with well-defined core–shell morphologies.[26]

Due to the slow chain exchange among micelles, the slow kinetics of block copolymers (usually with high molecular weight) in solution hinders assembled microstructures from reaching a global equilibrium state, thus forming a non-ergodic array of aggregates.[27,28] Some intermediate aggregate morphologies have been kinetically trapped, taking advantage of the slow kinetics of intermicellar interactions through infrequent intermicellar single-chain exchange.[29] The metastability of the assembly, strongly depending on the pathway of the system on the free energy landscapes, can give rise to variety of complex microstructures which can not be achieved in the equilibrium state.[12,28,30] Thus, it is desirable to obtain unique microstructures through trapping non-equilibrium intermediate structures when

*Hubei Key Lab of Materials Chemistry and Service Failure, School of Chemistry and Chemical Engineering, Huazhong University of Science and Technology, Wuhan, 430074, China. E-mail: jtzhu@mail.hust.edu.cn*

† Electronic supplementary information (ESI) available: Additional SEM and optical micrographs, BET spectrum of the hybrid particles, and movies showing the formation process of the hybrid microparticles. See DOI: 10.1039/c2sm06874e

coupled with the sol–gel chemistry of metal oxide precursor or increasing the viscosity of the fluids.

Interestingly, myelin-like structures could be formed when solid amphiphilic membranes were brought in contact with water upon dissolution of the amphiphiles.[31] These metastable intermediate structures can be kinetically trapped through sol–gel reactions when coupled with the spontaneous formation of myelin-like tubular structures of the amphiphilic diblock copolymer, poly(ethylene oxide)-*b*-poly(1,2-butylene oxide) (PEO–PBO).[32] The myelin outgrowths, which are a metastable intermediate state between the gel-like lamellar phase and dispersed multilamellar vesicles, are trapped in the form of highly anisotropic silica–polymer hybrid nanotubes by the addition of silica precursor tetraethylorthosilicate (TEOS) to the polymer gel before immersion in water. As a consequence, the continuous outgrowth of the multilamellar myelin filaments is concurrent with silica deposition at the polymer/water interface to produce mineralized replicas of the emergent nanostructures.[32] Recently, we have described an approach for the formation of amphiphilic block copolymer micelles and hierarchically-structured microparticles that takes advantage of hydrodynamic instabilities of the interface between organic solvent droplets and water.[33–37] In short, the polymers are first dissolved in a volatile, water-immiscible solvent (*e.g.*, chloroform), and this solution is dispersed as emulsion droplets in water. Removal of the organic solvent leads to the spontaneously increases in interfacial area and assembly of the copolymer into micellar or microparticulate structures. The driving force for the interfacial instabilities has been ascribed to the vanishing of the interfacial tension due to the adsorption of amphiphilic block copolymer polystyrene-*b*-PEO (PS–PEO) to the organic/water interface.[38–40] On the basis of the appearance of intermediate structures traced during the morphology evolution, the instabilities process is fairly slow (several to tens of minutes) due to relatively low mobility of the block copolymers and thus preservation of intermediate microstructures is possible.

In this report, we present a facile, yet versatile emulsion-based approach for the synthesis of organic–inorganic hybrid microstructures with an unprecedented control in texture and morphology, taking advantage of the interfacial instabilities of emulsion droplets containing amphiphilic copolymer PS–PEO and the sol–gel chemistry of the metal oxide precursors. The morphology of the hybrid microparticles can be effectively tuned by varying the amount of TEOS and the rate of solvent evaporation. Moreover, a small amount of titanium oxide precursor (tetra-*tert*-butyl orthotitanate, *e.g.*, TBOT) added together with TEOS to the initial emulsions leads to a fast hydrolization rate, allowing the preservation of the intermediate structures of the interfacial instabilities by solidification of the particle's shell with titanium oxide and silica. These kinetically trapped intermediate microstructures are interesting and helpful for the understanding of the aggregate morphology transition and the formation mechanism. This work might throw light on the research of the mechanism of biomineralization and give rise to the novel biomimetic strategies for producing complex hierarchically-structured materials, as the formed hybrid microstructures are similar to the naturally occurring spore particles of *Lycopodium clavatum*.[41,42]

## Experimental section

### Materials

$PS_{38k}$–$PEO_{11k}$ (with a PS number-average molecular weight of 38 000 g $mol^{-1}$ and a PEO weight of 11 000 g $mol^{-1}$, and polydispersity index of 1.06) was purchased from Polymer Source Inc. Poly(vinyl alcohol) (PVA, $M_w$ = 13–23k, 87–89% hydrolyzed) was purchased from Sigma-Aldrich. Chloroform (purity ≥ 99%) and TEOS (purity ≥ 99%) were purchased from Sinopharm Chemical Reagent Co., Ltd. while TBOT (purity ≥ 99%) was obtained from Kermel Chemical Reagent Co., Ltd, Tianjin, China. All the chemicals were used after receiving without further purification.

### Sample preparation

In a typical experiment, 10 mg $mL^{-1}$ PS–PEO and metal oxide precursors (TEOS or mixtures of TEOS and TBOT) at the desired concentration were dissolved in chloroform, and the solution (~20 μL) was mixed with deionized water containing 5 mg $mL^{-1}$ PVA (ranging from 0.5 to 3 mL), followed by simply shaking by hand. The chloroform was then allowed to evaporate by leaving the emulsion droplets (initial diameter: ~10–120 μm) in a small evaporation device (see Fig. 1(a)), which can be used to control the rate of solvent evaporation by varying the water layer height (*h*), open to air at room temperature. The device was prepared by gluing the glass slide with a plastic tube (inner diameter: ~21.5 mm). As we added 0.5 or 2 mL emulsions to the

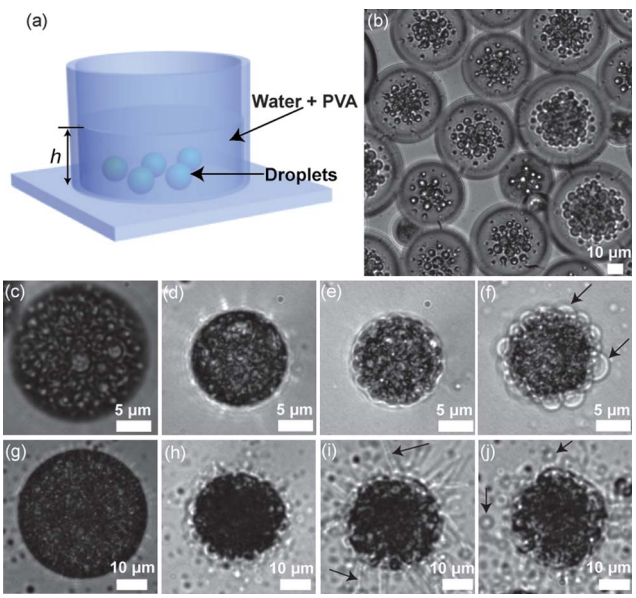


**Fig. 1** (a) Illustration of the experimental setup for controlling solvent evaporation rate; (b) optical micrograph of the as-formed emulsion droplets; (c–j) optical micrographs showing the evolution of the emulsions during chloroform evaporation. The same droplet seen in (c) remains in the images (d–f), which are taken (d) 23, (e) 29, and (f) 39 min after (c). The same droplet seen in (g) remains in the images (h–j), which are taken (h) 147, (i) 154, and (j) 179 min after (g). *h* varied from ~1.4 (c–f) to ~5.5 mm (g–j). The emulsion droplets consist of 10 mg $mL^{-1}$ $PS_{38k}$–$PEO_{11k}$ and 0.15 mol $L^{-1}$ TEOS. 5 mg $mL^{-1}$ PVA was added to the aqueous phase, where $NH_3 \cdot H_2O$ was added to adjust the pH value to 10.

evaporation device, $h$ would vary from ~1.4 to ~5.5 mm. With the increase of $h$, the diffusion distance of the organic solvent will thus increase, leading to a slower evaporation rate. In order to adjust pH value of the aqueous phase, ~80 μL ammonia water ($NH_3 \cdot H_2O$) was added to the PVA aqueous solution.

### Characterization

The evaporation process of the emulsion droplets was monitored by an inverted optical microscope (Olympus IX71). The resulting microparticles formed from interfacial instabilities of shrinking solvent droplets were characterized using an optical microscope and field-emission scanning electron microscope (SEM, Sirion 200) operated at an accelerated voltage of 10 kV. The elements for the selected area of the samples were probed by the energy-dispersive X-ray analysis (EDX) accessory to the SEM. To prepare the samples for the SEM, the particles aqueous suspension was dispersed on a clean silicon wafer and water was allowed to evaporate, followed by coating a thin layer of gold on the samples.

Fourier transform infrared (FT-IR) spectroscopy measurements were performed on a Bruker Vertex 70 FT-IR spectrometer in the wavenumber range of 400–4000 $cm^{-1}$ under ambient conditions. To prepare the samples for FI-IR, the dried hybrid microparticles were cast onto a KBr pellet. Powder X-ray diffraction (XRD) was carried out for identification of the crystalline phase of the inorganic framework. The XRD phase analysis (X'Pert PRO) was conducted on dried microparticles, and $2\theta$ varied over a range of 10–80°. Specific surface area, $N_2$ adsorption isotherms (77.2 K), and pore size distributions of the hybrid particles were measured by using Micromeritics ASAP2020M surface area and porosity analyzer. Before analysis, the samples were degassed at 50 °C for 8 h under vacuum ($10^{-5}$ bar). Thermogravimetric analysis (TGA) measurements, undertaken on dried particle samples, were performed on a PerkinElmer instrument Pyris Diamond 6300 TG/DTA Thermal Analyzer with a thermobalance at a heating rate of 15 °C $min^{-1}$ from 30 to 600 °C under an oxygen atmosphere. The observed mass loss was attributed to the quantitative pyrolysis of the polymeric component.

## Results and discussion

### Hybrid microparticles incorporated with $SiO_2$

We have used the small device to control the rate of solvent evaporation by simply varying $h$, as displayed in Fig. 1(a). With the increase of $h$, the diffusion distance of the organic solvent from the emulsion droplets to the water/air interface will thus increase, leading to a slower evaporation rate. As shown in Fig. 1(c–f), a fast solvent evaporation rate was achieved by setting $h$ to ~1.4 mm. Upon removal of chloroform, the organic/water interface became rough and the initially formed microstructures were too small to be resolved clearly by optical microscope, as shown in Fig. 1(d). The roughness would enlarge and bud-like microstructures appeared on the surface of the particles (Fig. 1(e)), which eventually formed budding vesicles (Fig. 1(f)). The whole process can also be resolved from Movie S1, ESI†. The process by which these budded particles form may be related to the budding mechanism of lipid/block copolymer vesicles.[43–45] We note that the process is also consistent with the previous report for the system without TEOS addition through microfluidic processing in which the final result is the PS–PEO microparticles coated with ~1μm sized "budding vesicles" on the particles surfaces.[33] The vesicular buds then gradually grew as a result of the interfacial instabilities of the emulsion droplets, followed by the hydrolysis/condensation of the silica precursors on the internal and external surfaces of the vesicles. Significantly, our control experiments undertaken in the absence of TEOS indicated that similar interfacial instabilities and final microparticles were also obtained under the above synthesis conditions, as shown in the ESI†, Fig. S1.

However, a qualitatively different mechanism of the interfacial instabilities was observed when $h$ was increased to ~5.5 mm to allow a slow solvent evaporation rate. Upon solvent removal, the droplets would shrink first (as shown in Fig. 1(g–j)), and the surface of the oil droplet started to become corrugated within ~147 min (Fig. 1(h)). We observed the growth of small liquid-filled spines extruding from the surface of the oil droplet, as shown in Fig. 1(i) (also see Fig. S1 and S2, ESI†). The spines sometimes reached a length of approximately ~50 μm, while typical lengths ranged from ~5 to 30 μm. Upon reaching a critical size, the spines started to tie up and formed a corona of submicroscopic vesicles around the oil droplets (see Fig. 1(j)). However, the details of the transition process between the spines and the vesicles can not be resolved clearly by optical microscopy. Surprisingly, the final structures were also budding vesicles (Fig. 2, Fig. S3(a) and S3(b), ESI†). The whole process lasted for ~200 min and can be observed in Movie S2, ESI†. Although the mechanism of the spines-to-vesicles transition needs to be further investigated, signs of the transition have been traced by the optical microscopy observations and SEM analysis (Fig. 1(g–j), Fig. S1 and S2, ESI†). SEM images indicated that the big vesicles (~5 μm and larger) on the surfaces of the particles would collapse due to the high vacuum during sample preparation (~$8e^{-5}$ mbar) and analysis (~$5e^{-5}$ mbar) while small buds (~1 μm and lower) would remain intact (Fig. S3(a), S3(b), and Fig. S4, ESI†). Compared the above two routes, the final structures were all microparticles with buds on their surfaces although the formation processes were quite different. Generally, the initial concentration of PS–PEO within the chloroform phase in each emulsion droplet was spatially uniform. Yet, an excess of PS–PEO will accumulate at the oil/water interface at fast solvent evaporation rates, especially when the shrinking speed becomes comparable to or greater than the PS-PEO diffusion rate. In this case, the accumulated PS–PEO molecules near the interfaces do not gain enough time to diffuse back to the bulk droplet and recover the uniform distribution. The droplet may develop a higher polymer concentration at the oil/water interface, and the increased near-surface concentration will trigger the interfacial instabilities at a lower average amphiphilic polymer concentration. Thus, the critical concentration of PS–PEO at the onset of the interfacial instabilities varied with the evaporation rate—a higher evaporation rate will shift the critical polymer concentration to a lower value. The varied critical polymer concentration will presumably modify the curvature of the assembly structures, eventually leading to the above different mechanism of the interfacial instabilities.

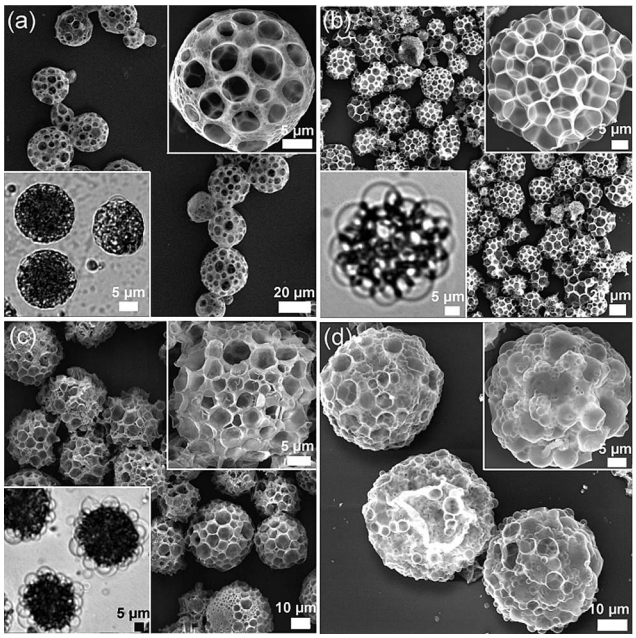


**Fig. 2** SEM images of the hybrid microparticles with various morphologies, formed from emulsion droplets containing 10 mg $mL^{-1}$ $PS_{38k}$–$PEO_{11k}$ and: (a) 0.15 mol $L^{-1}$ TEOS, microparticles with thin shell and macropores; $SiO_2$ content in the hybrid particles was 3.7 wt% from TGA measurement. (b–c) 0.3 to 0.6 mol $L^{-1}$ TEOS, microparticles with faviform pores; $SiO_2$ content in the hybrid particles was 5.7 wt% and 17.8 wt%, respectively. (d) 0.75 mol $L^{-1}$ TEOS, microparticles with vesicles on the surface, $SiO_2$ content in the hybrid particles was 19.8 wt%. *h* was set to ~5.5 mm while the pH value of the aqueous solution was 10. Insets in the upper right are the enlarged SEM images while insets in the lower left are the corresponding optical micrographs of the particles in aqueous suspension. The optical micrographs were taken 1 day after the evaporation process to make sure that interfacial instabilities were completed and the particles were stable.

The challenge here is to preserve the metastable dendritic microstructures by coupling the mineralization process of TEOS to the interfacial instabilities process of the emulsion droplets. In our previous report, we have tried to add hydrophobic homopolymer PS to the initial PS–PEO solution to slow down the kinetics of the system by increasing the fluids viscosity and trap the microstructures in an earlier stage of the instabilities.[33] Dendritic particles, where cylindrical protrusions of 1–3 μm in length coated the particles (overall diameter: ~3 μm), were obtained through this process. In this work, we have tried to employ a different strategy to trap the intermediate structures of the interfacial instabilities. Specifically, we add TEOS to the initial chloroform droplets which will hydrolyze and condense into silica at the organic/water interface during solvent removal, preventing reorganization of the assemblies into equilibrium structures by kinetically trapping the intermediate microstructures. To induce the presence of the fluid spines effectively, we employed higher water layer height of ~5.5 mm in the evaporation device to achieve slow solvent evaporation rate.

To establish the effect of the hydrolization/condensation of TEOS on the morphologies of the hybrid microparticles, we test TEOS content effect on the interfacial instabilities and the final particle morphologies. Cage-like microparticles with cavities of tens of nanometres to several microns were obtained when the TEOS concentration was 0.15 mol $L^{-1}$, as displayed in Fig. 2(a). Whereas a higher silica precursor content (0.3 mol $L^{-1}$) gave rise to highly porous microparticles (honeycomb-like particles with connected cavities with sizes of ~5 μm), as shown in Fig. 2(b). EDX analysis on the microparticles was taken and the results confirmed that the Si peak at 1.7 e kV appeared (Fig. 3(a)). Interestingly, the microparticles showed a substantial similarity to a naturally occurring spore particle, called *Lycopodium clavatum*.[41] Due to its rough surface structures, these microparticles could act as efficient stabilizers of oil and water. When the TEOS concentration was increased to 0.6 mol $L^{-1}$, porous microparticles with concave structures in the pores were produced, as displayed in Fig. 2(c). It is worth noting that the porous microparticles in Fig. 2(a–c) originated from budding vesicles with bud sizes of several microns in aqueous suspensions, as can be seen from the corresponding optical microscopy images in the insets of the figures. The differences between these SEM images and the corresponding optical microscopy images largely result from the stability of the initially integrated buds in the vacuum during the sample preparation and analysis, which in turn depends on the amount of silica deposited around them and hence the TEOS concentration. Further increase in silica content resulted in microparticles with integrated buds on the particle surface due to excess silica mineralization on the external and internal surfaces of the polymer particles, as shown in Fig. 2(d) (also see Fig. S4, ESI†). These microparticles displayed interconnected porous internal structures, as can be resolved from the broken microparticles in Fig. 4(a) and 4(b). The reason for the cavities inside the particles is thought to originate from the trapped water droplets stabilized by PS–PEO during the emulsions preparation (see Fig. 1(b) and Fig. S1, ESI†). Removal of the polymer component from the hybrids in Fig. 2(b) and 2(c) to produce intact silica replicas was achieved by heating the samples up to 400 °C for 4 h. As supported by the SEM images in Fig. 4(c) and 4(d), thermal treatment did not disturb the macroscopic shape and the internal morphology of the aggregates significantly, although partial degradation of the internal structures was unavoidable. These results were also confirmed by THF elution treatment on the microparticles, whereby the polymers were extracted with THF and similar structures were obtained, as shown in Fig. 4(e) and 4(f). Because of the mechanical and physical robustness of the inorganic networks, the aggregates are stable and shape-persistent.

The formation of integrated silica–polymer composites was confirmed by FT-IR spectroscopy, as shown in Fig. 3(b). The FT-IR spectrum of the hybrid material showed typically strong vibration peaks for PS–PEO/$SiO_2$, for example at 1098 $cm^{-1}$ [polymer (C–O–C) and Si–O–Si)] and 2875–2964 $cm^{-1}$ (polymer, $CH_2$, $CH_3$). The FT-IR analysis indeed confirms the organic/inorganic hybrid nature of the composites. To get some information on the $SiO_2$ in the microparticles after calcination, we analyzed some samples by XRD, as displayed in Fig. 3(c). The XRD pattern for the powder sample showed only a very broad peak centered at $2\theta = 22°$, indicating that the particles were amorphous. Thermogravimetric analysis (TGA) is useful for determining the content of inorganic components in composite materials. A typical TGA curve of the composite, as an example,

 

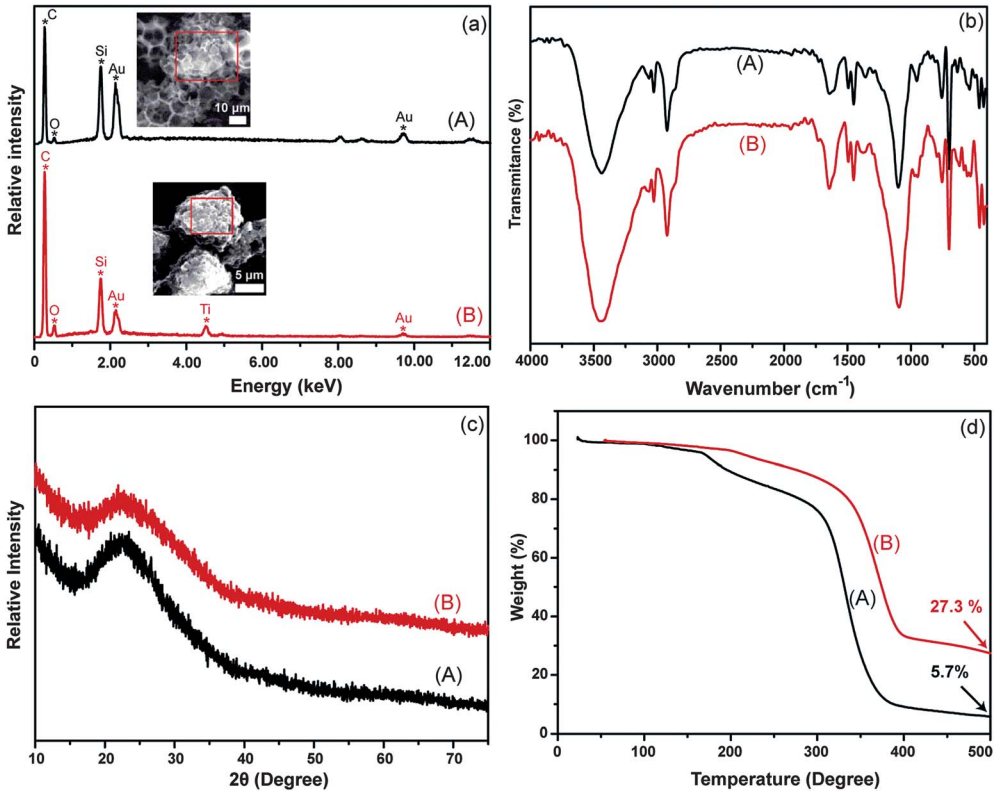


**Fig. 3** EDX (a), FTIR (b), XRD (c), and TGA (d) spectra of the hybrid microparticles formed from emulsion droplets containing 10 mg $mL^{-1}$ $PS_{38k}$–$PEO_{11k}$ and: (A) 0.3 mol $L^{-1}$ TEOS at pH = 10; (B) 0.3 mol $L^{-1}$ TEOS and 1.5 μmol $L^{-1}$ TBOT at pH = 10. In (a) the insets are the corresponding SEM images, and the areas marked with red squares were selected for EDX analysis. We note that gold signal originated from the thin gold layer coating on the samples before analysis to prevent charging. As shown in (b), the FT-IR spectra of the hybrid copolymer–silica particles, for example, contains IR bands that are characteristic of both a silica network (1098 $cm^{-1}$, multiplet corresponding to Si–O stretching; 952 $cm^{-1}$, Si–OH vibration mode; 806 $cm^{-1}$, Si–O–Si bending; 463 $cm^{-1}$, Si–O bending) and also to the copolymer (1098 $cm^{-1}$, C–O–C stretching for the polymer; 2875–2964 $cm^{-1}$ vibration for the polymer $CH_2$ and $CH_3$).

is given in Fig. 3(d). The result shows a loss of 10.7 wt%, below 200 °C, which is assigned to the release of water physisorbed on the composites. From 200 to 500 °C, there is an obvious decrease in weight which can be ascribed to the decomposition of the polymer in the composite. Obviously, the content of $SiO_2$ in the copolymer–$SiO_2$ hybrid was 5.7 wt%, as can be seen from TGA curve in Fig. 3(d). Brunauer–Emmett–Teller (BET) analysis of the hybrid microparticles indicated that the specific surface area for the porous microparticles (~17 $m^2$ $g^{-1}$) is much higher than that for solid microparticles with smooth surfaces (~2 $m^2$ $g^{-1}$), as displayed in ESI†, Fig. S5.

The above results indicated that hybrid microparticles with multiple morphologies were obtained by varying the content of TEOS and the rate of solvent evaporation. This provides us with a new strategy to prepare hybrid microparticles with hierarchical structures. However, from the above discussion, fluid spines encountered at the early stages of interfacial instabilities have not been successfully trapped and preserved with TEOS mineralization. Presumably, this is due to the slow hydrolysis/condensation process of TEOS, and most of which were taken when the microstructures were fixed after complete removal of chloroform.[46] In this case, more stable polymer assemblies of the budding vesicles would be produced and most of the $SiO_2$ was formed after microparticles formation.

### Hybrid microparticles incorporated with $SiO_2$ and $TiO_2$

A major improvement was achieved by employing TBOT or a mixture of TBOT/TEOS that are hydrolytically less stable than typical silica precursors.[46] By using admixtures of TBOT and TEOS, we were able to preserve the intermediate microstructures of the interfacial instabilities by forming mineralized shells at the oil–water interface. The early stages of the interfacial instabilities were designed to be fixed for further observation. By doing so, we added 0.3 mol $L^{-1}$ TEOS and 1.50 μmol $L^{-1}$ TBOT together with PS–PEO to the initial chloroform. Ammonia water was added to the aqueous phase to adjust the pH value to 10. With the fast rate of chloroform evaporation ($h$ = ~1.4 mm), similar multi-porous microparticles can be obtained as discussed above by adding TEOS (as shown in Fig. 2(b)). When the evaporation rate was adjusted to a adequate ($h$ = ~5.5 mm), the fluid spines grew out from each droplet were fixed before reorganization into budding vesicle structures. From the SEM images in Fig. 5(a), the dendritic or wormlike structures can be seen clearly on the surface of the microparticles. Such structures represent intermediate forms associated with the transformation of spines into vesicles in the presence of a relatively large water layer height. Presumably, during solvent evaporation, the filaments grew and hydrated PEO microdomains in the filaments will rearrange and

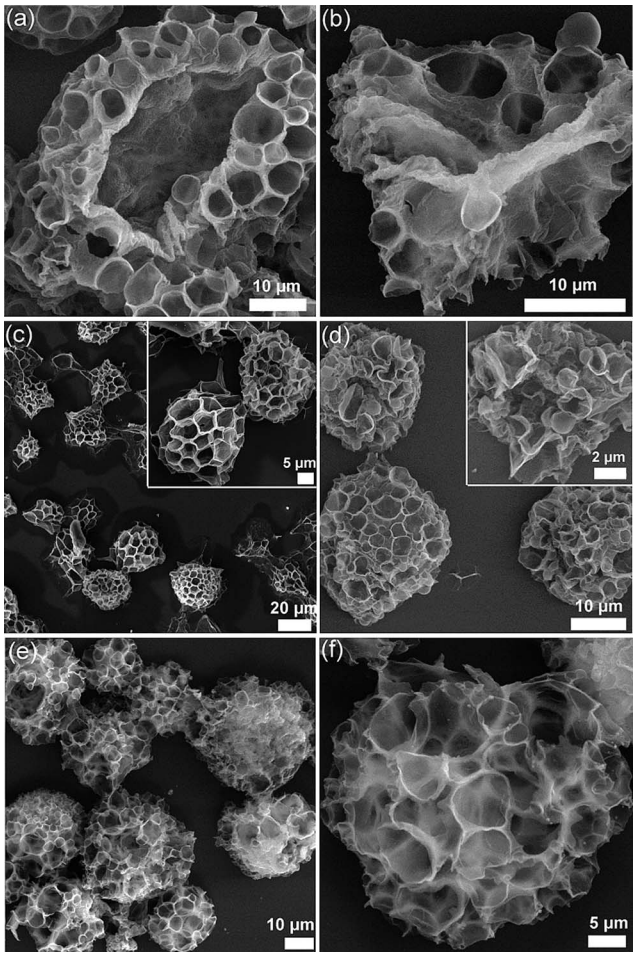


**Fig. 4** (a–b) SEM images of crushed hollow microparticles. (c–f) SEM images of microparticles after being heated at 400 °C for 4 h to remove the copolymers (c, d) or eluted with THF for 1 day (e, f). The hybrid microparticles were formed from emulsion droplets containing 10 mg mL$^{-1}$ $PS_{38k}$–$PEO_{11k}$ and: (a–c, e) 0.3 mol L$^{-1}$ TEOS at pH = 10; (d, f) 0.6 mol L$^{-1}$ TEOS at pH = 10.

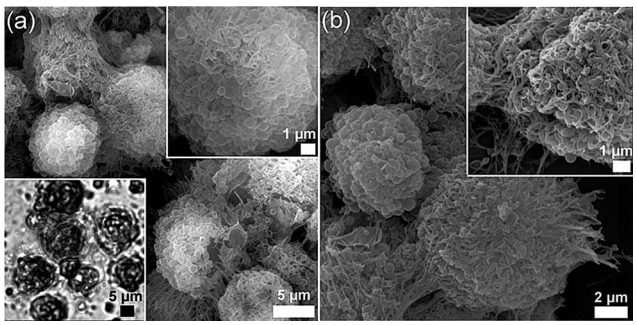


**Fig. 5** SEM images of the hybrid aggregates formed from emulsion droplets containing 10 mg mL$^{-1}$ $PS_{38k}$–$PEO_{11k}$, 0.3 mol L$^{-1}$ TEOS, and 1.5 μmol L$^{-1}$ TBOT at pH 10. Clearly, dendritic microparticles coated with small vesicles and cylinders were formed. (b) is the SEM image of the corresponding microparticles after calcination at 400 °C for 4 h. In the sample preparation, *h* was set to ~5.5 mm. Insets in the upper right are the enlarged SEM images while inset in the lower left is the corresponding optical micrograph of the particles.

form hollow structures (*e.g.*, vesicles) without TBOT addition, as described above. As shown in Fig. 5(b), the microstructures can be maintained after heating the samples up to 400 °C for 4 h. Clearly, a small amount of added TBOT can allow us to successfully preserve the intermediate microstructures of the interfacial instabilities. Co-addition of TBOT allowed for the replication of an earlier stage of the spines due to the faster hydrolysis kinetics. Moreover, we find that silica precursor concentration and pH value of the aqueous phase play important role in influencing the interfacial instabilities as well as the structures of the hybrid microparticles, as shown in the ESI†, Fig. S6 and Fig. S7.

The formation of integrated silica–polymer and titania–polymer composites was confirmed by FT-IR spectroscopy (shown in Fig. 3(b)) while the XRD pattern for the powder sample in Fig. 3(c) indicated that the microparticles after calcination were also amorphous. The obvious characteristic peaks for C, O, Si, and Ti, originating from the composite microparticles, are found in the EDX spectrum located at the surface of discrete particle in Fig. 3(a), indicating that $SiO_2$ (peak at 1.7 keV) and $TiO_2$ (peak at 4.3keV) are indeed incorporated into the hybrid microparticles. Furthermore, weight fraction of the $TiO_2$ in the $TiO_2$/$SiO_2$ mixture was estimated to be 28.9% based on the EDX data in Fig. 3(a). TGA analysis indicated that the metal oxide (*e.g.*, $SiO_2$ and $TiO_2$) of these hybrid copolymer–silica particles was about 27.3 wt% by mass (see Fig. 3(d)), indicating that small amount of TBOT addition can significantly improve the $SiO_2$ mineralization in the emulsion droplets.

## Hybrid nanostructures

Furthermore, we have investigated the effect of the concentration of water-soluble surfactant PVA on the assembly morphology. Generally, PVA acts as a surfactant to stabilize the emulsion droplets. When increasing PVA concentration to 50 mg mL$^{-1}$, qualitatively different mechanisms of the interfacial instabilities were observed for the emulsion droplets containing PS–PEO, TEOS, and TBOT—fluid spines would grow out continuously and hybrid wormlike micelles were formed, as shown in Fig. 6. Although the dominating structure was the isolated wormlike micelles, bunches of cylindrical aggregates were occasionally observed, as indicated by arrows in Fig. 6(a) and 6(b). As the PVA concentration increases, the adsorption of water-soluble surfactant PVA to the organic–water interface lowers the interfacial tension, thereby reducing the concentration of amphiphilic copolymer necessary to approach zero interfacial tension and driving the interface instabilities.[35] Also, PVA further modifies the interfacial instabilities mechanism while an increasing amount of adsorbed PVA causes a shift to high-curvature structures (from bilayer to cylindrical structures) in a similar way as increasing the hydrophilic content of the block copolymer.[35] As shown in the inset TEM image in Fig. 6(c), the cylinders are solid with rough surfaces, ~100 nm in diameter and ~4 μm in length. The structures can also be maintained after being heated to 400 °C for 4 h, as shown in the SEM image in Fig. 6(d). After elution with THF, which is a good solvent for PS–PEO, the cylinders become hollow, which can be seen clearly in the inset of Fig. 6(d) for the TEM image. The surface roughness (tiny spots) can be ascribed to the inorganic nanoparticles.

 

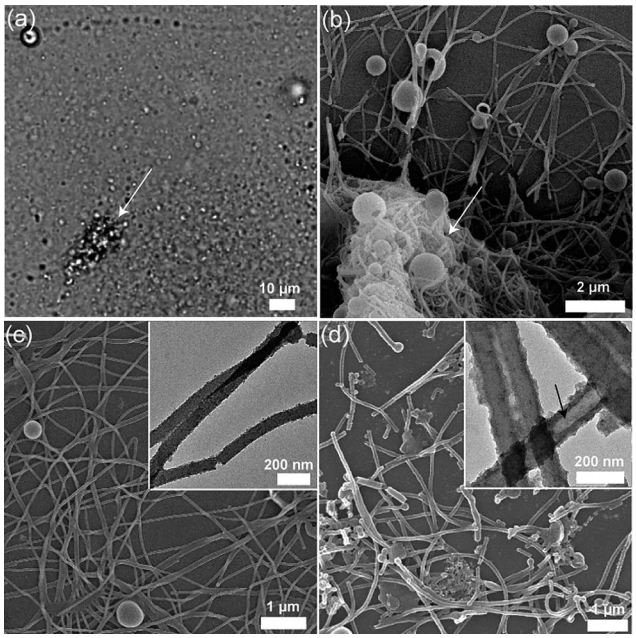


**Fig. 6** Optical micrograph (a) and SEM image (b) of the hybrid wormlike micelles. Cylindrical aggregates are occasionally encountered, as indicated by arrows in (a) and (b). (c, d) SEM images of the hybrid wormlike micelles (c) before and (d) after calcination. The hybrid wormlike micelles were formed from emulsion droplets containing 10 mg $mL^{-1}$ $PS_{38k}$–$PEO_{11k}$, 0.3 mol $L^{-1}$ TEOS, and 1.5 μmol $L^{-1}$ TBOT with 50 mg $mL^{-1}$ PVA in the aqueous solution at pH 10. *h* was set to ~5.5 mm. The inset in (c) is a representative TEM image for the hybrid wormlike micelles while the inset in (d) shows the hybrid silica–titania nanotubes after dissolution with THF to remove the copolymers.

These $TiO_2$–$SiO_2$ hybrid nanotubes might find application in the areas of catalysis, sensors, and device fabrication. While a control experiment undertaken in the absence of TEOS and TBOT indicated that cylinders or strings-of-vesicles were obtained under the above conditions.[35] It is worthy to note that similar silica tubular structures were reported based on the *in situ* mineralization of myelin outgrowths. However, the differences between the wormlike structures described in this work and the myelin figures are obvious. Besides the wormlike tubes, twisted nanotubes, budded filaments, as well as peal-like nanotubes with diameters of 200–250 nm were also observed for the myelin outgrowth. Yet, the nanotubes demonstrated here are more straight and smooth on the surfaces. Given the mild conditions, fast reaction time, and tunable assemblies with only one polymer, such a kinetic self-assembly approach appears to offer some advantages over conventional template synthesis on the composite formation. Moreover, the final hybrid copolymer–silica particles are expected to be reasonably biocompatible, and the inorganic shell is expected to offer a more effective diffusion barrier for the long-term entrapment of hydrophobic additives within the cylinders' cores.

The morphological formation and evolution observed in the present study is obviously complicated by the multiplicity of factors involved, *i.e.*, the rate of solvent evaporation, TEOS and/or TBOT content, self-assembly of PS–PEO, surfactant concentration, and the sol–gel chemistry of metal oxide precursors. All these factors influence the observed instabilities and morphologies of the hybrid materials. In order to trap the intermediate structures, the silicate chemistry needs to take place simultaneously with the interfacial instabilities of the emulsion droplets. The above results illustrate the potential for controlling the functionalization of polymer–inorganic nanotubes prepared by kinetic co-assembly of amphiphilic block copolymers and metal oxide precursors. Indeed, the use of kinetically-trapped nanostructures opens up the possibility of producing unique hierarchical composites that are hard to produce by the traditional approach.

## Conclusion

We demonstrate the successful synthesis of PS–PEO/silica hybrid microparticles with multiple morphologies by coupling the self-assembly of PS–PEO in emulsion droplets with the sol–gel chemistry of silica precursors. By manipulation of the rate of solvent evaporation, concentration of the inorganic precursors, and concentration of the surfactant, hybrid particles with varied morphologies (*e.g.*, cage-like, honeycomb-like, dendritic microparticles, and wormlike micelles) were produced by taking advantage of the interfacial instabilities of emulsion droplets. The early stages of the instabilities can be kinetically trapped by adding a small amount of TBOT, which will shed light on the study the mechanism of the interfacial instabilities. This non-equilibrium pattern formation derives from the interplay between the competitive and cooperative processes of self-assembly and sol–gel chemistry of the precursors. We anticipate that this kinetic self-assembly strategy may also be generally applicable to the synthesis of other functional materials with hierarchical structures and complex morphologies. Moreover, the mechanism of the kinetic co-assembly of block copolymers with silica might be enlightening to the functional properties of these macromolecules in biological systems.[42,47]

## Acknowledgements

We grateful acknowledge funding for this work provided by the National Natural Science Foundation of China (21004025), Chinese Ministry of Education (NCET-10-0398), and the Fundamental Research Funds for the Central Universities (HUST: 2010MS081). We also thank HUST Analytical and Testing Center for allowing us to use its facilities.

## Notes and references

1 D. E. Discher and A. Eisenberg, *Science*, 2002, **297**, 967–973.
2 S. Jain and F. S. Bates, *Science*, 2003, **300**, 460–464.
3 H. B. Du, J. T. Zhu and W. Jiang, *J. Phys. Chem. B*, 2007, **111**, 1938–1945.
4 T. Smart, H. Lomas, M. Massignani, M. V. Flores-Merino, L. R. Perez and G. Battaglia, *Nano Today*, 2008, **3**, 38–46.
5 J. W. Hu, G. J. Liu and G. Nijkang, *J. Am. Chem. Soc.*, 2008, **130**, 3236–3237.
6 Z. B. Li, E. Kesselman, Y. Talmon, M. A. Hillmyer and T. P. Lodge, *Science*, 2004, **306**, 98–101.
7 X. S. Wang, G. Guerin, H. Wang, Y. S. Wang, I. Manners and M. A. Winnik, *Science*, 2007, **317**, 644–647.
8 J. T. Zhu, H. Z. Yu and W. Jiang, *Eur. Polym. J.*, 2008, **44**, 2275–2283.
9 S. Mann, *Nat. Mater.*, 2009, **8**, 781–792.
10 L. F. Zhang and A. Eisenberg, *Polym. Adv. Technol.*, 1998, **9**, 677–699.

11 C. Mugemana, P. Guillet, C. A. Fustin and J. F. Gohy, *Soft Matter*, 2011, **7**, 3673–3678.
12 H. G. Cui, Z. Y. Chen, S. Zhong, K. L. Wooley and D. J. Pochan, *Science*, 2007, **317**, 647–650.
13 S. C. Warren, F. J. Disalvo and U. Wiesner, *Nat. Mater.*, 2007, **6**, 156–161.
14 C. Sanchez, H. Arribart and M. M. G. Guille, *Nat. Mater.*, 2005, **4**, 277–288.
15 N. Andersson, B. Kronberg, R. Corkery and P. Alberius, *Langmuir*, 2007, **23**, 1459–1464.
16 R. Schiller, C. K. Weiss, J. Geserick, N. Husing and K. Landfester, *Chem. Mater.*, 2009, **21**, 5088–5098.
17 M. Müllner, J. Y. Yuan, S. Weiss, A. Walther, M. Förtsch, M. Drechsler and A. H. E. Müller, *J. Am. Chem. Soc.*, 2010, **132**, 16587–16592.
18 L. Li, Y. W. Zhong, C. Y. Ma, J. Li, C. K. Chen, A. J. Zhang, D. L. Tang, S. Y. Xie and Z. Ma, *Chem. Mater.*, 2009, **21**, 4977–4983.
19 J. Fan, S. W. Boettcher, C. K. Tsung, Q. Shi, M. Schierhorn and G. D. Stucky, *Chem. Mater.*, 2008, **20**, 909–921.
20 G. Tan, P. Xu, J. B. He, L. Lawson, G. L. McPherson and V. T. John, *Soft Matter*, 2009, **5**, 3006–3009.
21 H. Zou, S. S. Wu and J. Shen, *Chem. Rev.*, 2008, **108**, 3893–3957.
22 A. Khanal, Y. Inoue, M. Yada and K. Nakashima, *J. Am. Chem. Soc.*, 2007, **129**, 1534–1535.
23 Y. Zhang, H. Tan, H. Li, Y. Q. Liu, F. C. Kartawidjaja, Z. C. Yang and J. Wang, *Chem. Mater.*, 2011, **23**, 2745–2752.
24 J. G. Wang, Q. Xiao, H. J. Zhou, P. C. Sun, Z. Y. Yuan, B. H. Li, D. T. Ding, A. C. Shi and T. H. Chen, *Adv. Mater.*, 2006, **18**, 3284–3288.
25 N. Baccile, J. Reboul, B. Blanc, B. Coq, P. Lacroix-Desmazes, M. In and C. Gerardin, *Angew. Chem., Int. Ed.*, 2008, **47**, 8433–8437.
26 J. J. Yuan, O. O. Mykhaylyk, A. J. Ryan and S. P. Armes, *J. Am. Chem. Soc.*, 2007, **129**, 1717–1723.
27 S. Jain and F. S. Bates, *Macromolecules*, 2004, **37**, 1511–1523.
28 J. T. Zhu, Y. Jiang, H. J. Liang and W. Jiang, *J. Phys. Chem. B*, 2005, **109**, 8619–8625.
29 Y. Y. Won, H. T. Davis and F. S. Bates, *Macromolecules*, 2003, **36**, 953–955.
30 K. Yu, C. Bartels and A. Eisenberg, *Langmuir*, 1999, **15**, 7157–7167.
31 G. Battaglia and A. J. Ryan, *Angew. Chem., Int. Ed.*, 2006, **45**, 2052–2056.
32 M. Li and S. Mann, *Angew. Chem., Int. Ed.*, 2008, **47**, 9476–9479.
33 J. Zhu and R. C. Hayward, *Angew. Chem., Int. Ed.*, 2008, **47**, 2113–2116.
34 J. T. Zhu and R. C. Hayward, *J. Am. Chem. Soc.*, 2008, **130**, 7496–7502.
35 J. T. Zhu, N. Ferrer and R. C. Hayward, *Soft Matter*, 2009, **5**, 2471–2478.
36 R. C. Hayward and D. J. Pochan, *Macromolecules*, 2010, **43**, 3577–3584.
37 J. T. Zhu and R. C. Hayward, *Macromolecules*, 2008, **41**, 7794–7797.
38 K. Chang, C. W. Macosko and D. C. Morse, *Macromolecules*, 2007, **40**, 3819–3830.
39 J. B. Jiao, E. J. Kramer, S. de Vos, M. Möller and C. Koning, *Macromolecules*, 1999, **32**, 6261–6269.
40 J. C. Lopez-Montilla, P. E. Herrera-Morales, S. Pandey and D. O. Shah, *J. Disper. Sci. Technol.*, 2002, **23**, 219–268.
41 B. P. Binks, J. H. Clint, G. Mackenzie, C. Simcock and C. P. Whitby, *Langmuir*, 2005, **21**, 8161–8167.
42 A. W. Xu, Y. R. Ma and H. Colfen, *J. Mater. Chem.*, 2007, **17**, 415–449.
43 J. C. M. Lee, H. Bermudez, B. M. Discher, M. A. Sheehan, Y. Y. Won, F. S. Bates and D. E. Discher, *Biotechnol. Bioeng.*, 2001, **73**, 135–145.
44 H. G. Dobereiner, J. Kas, D. Noppl, I. Sprenger and E. Sackmann, *Biophys. J.*, 1993, **65**, 1396–1403.
45 Y. F. Zhou and D. Y. Yan, *Angew. Chem., Int. Ed.*, 2005, **44**, 3223–3226.
46 T. Y. Peng, A. Hasegawa, J. R. Qiu and K. Hirao, *Chem. Mater.*, 2003, **15**, 2011–2016.
47 C. C. Perry and T. Keeling-Tucker, *J. Biol. Inorg. Chem.*, 2000, **5**, 537–550.

 